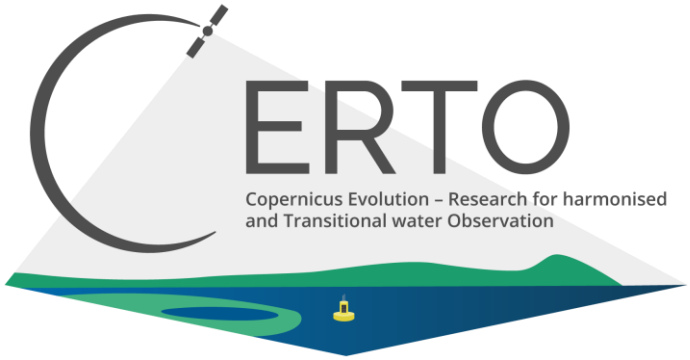

Horizon 2020

H2020 LC-SPACE-04-EO-2019-2020

Copernicus Evolution – Research for harmonised and Transitional-water Observation (CERTO)

Project Number: 870349

Deliverable No: D5.2		Work Package: 5	
Date:	12-JAN-2021	Contract delivery due date	31-DEC-2020
Title:	Radiative transfer simulation dataset and documentation		
Lead Partner for Deliverable	HYGEOS		
Author(s):	Didier RAMON, François STEINMETZ		
Dissemination level (PU=public, RE=restricted, CO=confidential)			PU
Report Status (DR = Draft, FI = FINAL)			DR

Acknowledgements

This project has received funding from the European Union's Horizon 2020 research and innovation programme grant agreement N° 870349

Table of Contents

1 Executive Summary

- This document describes the setup, computation and format of a database of radiative transfer simulations aiming at studying the impact of adjacency and bathymetry effects on the retrieved marine reflectances from remote sensing.
- For that purpose, the RTC Monte-Carlo code SMART-G has been parametrized and optimized for this specific large scale computation. The parameters of the simulations have been chosen in order to represent most of the natural variability of these two effects: (i) a wide range of spectral water types, (ii) typical range for aerosol load, altitude and aerosol model, (iii) typical spectral types of the land environment and seafloor and finally (iv) the average and extreme geometrical conditions encountered by the S3/OLCI and S2/MSI sensors in terms of view and solar zenith angles, relative azimuths between the Sun and the sensor and the sensor and the coastline, distance to the coast or radius of the inland water body and finally sea depth.
- The computations have been performed for the radiances at the top of atmosphere (TOA) and just above and below the wind roughened sea surface for all S3/OLCI and S2/MSI spectral bands including those with significant gaseous absorption. The results are written in several NetCDF files.

2 Introduction

Satellite sensor scenes exhibiting horizontal variations pose a problem in Radiative Transfer simulations. For atmospheric correction of ocean-colour imagery, it is generally assumed that the target is horizontally homogeneous, or equivalently that the target is infinitely large. This “large target” formalism is generally appropriate in the open ocean, sufficiently far from clouds and land, since the intrinsic atmospheric reflectance (i.e., the signal that has not interacted with the water body) is the main perturbing signal. In the vicinity of land, near sea ice or clouds, and even where horizontal heterogeneity is large (in the case of upwelling areas), the impact of photons reflected by the environment of the target and scattered into the field of view may not be negligible and may yield erroneous water reflectance retrievals and derived biogeochemical variables (Santer and Schmechtig, 2000). The problem is not only the adjacency effect at the wavelength of interest, i.e., ultraviolet to visible, but also (in some cases more importantly) the propagation to shorter wavelengths of errors in the determination of aerosol scattering in the red and near infrared. At these wavelengths the environment reflectance is seen in the atmospheric correction scheme as part of the aerosol reflectance. The atmospheric variables controlling the adjacency effect are the aerosol amount (optical thickness) and altitude, and to a lesser extent the aerosol model (Frouin et al., 2019).

3 Radiative Transfer Simulations

3.1 Radiative Transfer Code

SMART-G (Speed-up Monte-carlo Advanced Radiative Transfer code with GPU) is a radiative transfer solver for the coupled ocean-atmosphere system with a wavy interface [Ramon et al., 2019] or any surface spectral BRDF boundary condition. It is based on the Monte-Carlo technique, works in either plane-parallel or spherical-shell geometry, and accounts for polarization. The vector code is written in CUDA (Compute Unified Device Architecture) and runs on GPUs (Graphic Processing Units). Physical processes included in the current version of the code are the elastic scattering, absorption, reflection, thermal emission and refraction. Inelastic processes such as fluorescence and Raman scattering are currently under validation The atmosphere and ocean are considered as 1-dimensional stratified media with layers or 3-dimensional with cells characterized by gaseous optical depth and single scattering albedo (case of atmosphere), Rayleigh phase matrix, and particle (aerosol, hydrosol, and/or cloud droplet/crystal) optical depth, single scattering albedo, and phase matrix. The ocean can be infinitely deep or bounded by a BRDF reflective bottom at finite depth.

The ground interface can be modelled in two ways: (i) as a purely reflecting interface whose BRDF/BPDF is obtained by the combination of the isotropic wave slope distribution [*Cox and Munk*, 1954] or and the Fresnel reflection matrix in the case of the ocean or directly a reflexion matrix for the general case (for example a Ross-Thick Li-Sparse BRDF model for land surfaces). The direction of the reflected photons is sampled according to a lambertian law and the photon statistical weight is multiplied by the BRDF [Mayer, 2009], and (ii) by sampling the wave slope and azimuth according to a distribution law based on an azimuthally independent wave slope distribution [Cox and Munk, 1954] but now depending on the photon incident zenith angle [Plass et al., 1975]. This procedure results in some slopes hiding [Ross et al., 2005]. Then, Fresnel reflection (resp. transmission) is applied to

the reflected (resp. transmitted) photon Stokes vector. In both cases the light intensity is eventually modulated by a wave shadowing function [Mischenko and Travis, 1997b].

The radiances at any level of the domain can be estimated using the local estimate variance reduction method [Marchuk et al., 1980]. Benchmark values are accurately reproduced for clear [Natraj and Hovenier, 2012] and cloudy atmospheres [Kokhanovsky et al., 2010] over a wavy reflecting surface and a black ocean [Emde et al., 2015]. For pure Rayleigh atmospheres as in AOS comparisons, the agreement is better than 10^{-5} in intensity and 0.1% in degree of polarization [Ramon et al., 2019, Chowdhary et al., 2020].

One advantage of the SMART-G code is the possibility to introduce easily increasing complexity in the system, like, for example, wave heights, horizontal inhomogeneities of the albedo like adjacency effects [Chowdhary et al., 2019], or 3-dimensional variations of the oceanic/atmospheric optical properties. Its traditional drawbacks, the speed and Monte Carlo noise, is counterbalanced by the use of massive parallelization on GPU, which for a given machine typically speeds up by two orders of magnitude the computation time compared with a sequential algorithm running on CPUs.

Another advantage of the Monte Carlo code is a quick and easy computation of the coupling between absorption and scattering as described in [Emde et al., 2011]. The method is named ALIS and it is a very powerful method enabling SMART-G to be very fast compared to deterministic codes in the case of high spectral resolution computation.

The code has been validated against benchmark for the Rayleigh + sun glint test and is very fast compared to traditional CPU MC Code (~speed up factor of ~ 100 for 1 GPU vs 1CPU). In the context of a separate project (the ESA preparatory studies for the mission ALTIUS - Atmospheric Limb Tracker for Investigation of the Upcoming Stratosphere on-board a PROBA platform) SMART-G was selected in the last 3 RT codes allowing to perform accurate limb viewing polarized radiance computation including refraction. The global comparison exercise involved: SAKSTRAN-MC, SAKSTRAN-HR, MYSTIC, SIRO, SCIATRAN and SMART-G [Zawada et al., 2020].

3.2 Optical Properties

3.2.1 Spectral bands

Band	Central wavelength (nm)	FWHM (nm)
Oa01	399.9	14.0
Oa02	411.8	9.8
Oa03	442.9	9.9
Oa04	490.4	9.9
Oa05	510.4	9.9
Oa06	560.4	9.9
Oa07	620.4	9.9
Oa08	665.2	9.9
Oa09	674.0	7.4
Oa10	681.6	7.4
Oa11	709.1	9.9

Oa12	754.2	7.4
Oa13	761.7	2.5
Oa14	764.8	3.7
Oa15	767.9	2.5
Oa16	779.2	15.0
Oa17	865.6	19.8
Oa18	884.4	9.9
Oa19	899.4	9.9
Oa20	939.3	19.7
Oa21	1 012.9	26.9

Table 1: S3A OLCI spectral bands.

Band	Central wavelength (nm)	FWHM (nm)
MSI01	442.5	19.0
MSI02	492.0	64.0
MSI03	560.0	34.0
MSI04	664.5	29.0
MSI05	704.5	13.0
MSI06	740.5	13.0
MSI07	783.0	18.0
MSI08	835.0	104.0
MSI08a	864.5	19.0
MSI09	945.0	18.0
MSI10	1373.5	29.0
MSI11	1613.5	89.0
MSI12	2199.5	173.0

Table 2 S2A MSI spectral bands

3.2.2 Atmosphere

The aerosol optical properties are taken from the OPAC database (Hess et al., 1998) and the gaseous absorption is modelled according to REPTRAN (Gasteiger et al., 2014). They distributed within the libradtran software package (www.libradtran.org). Aerosols are supposed to be spherical. Rayleigh optical depth is computed according to Bodhaine et al., 1999.

3.2.2.1 Aerosols Models

The aerosols models built for this study are a mixture of OPAC aerosol components, and a vertical profile of the extinction coefficient that is decreasing exponentially with a scale height H_a:

$$k_{ext}(z) = k_{ext}(0)e^{-z/H_a}$$

For a given relative humidity RH, the fraction of each component i X_i within the mixture is defined as the column fractional optical depth at 550 nm:

$$X_i = \frac{AOD_i^{550}(RH)}{AOD^{550}(RH)}; i \in \{waso, ssam, sscm, inso, soot, minm, miam, micm\}$$

#	Type	RH (%)	H_a (km)	X_{waso}	X_{ssam}	X_{sscm}	X_{inso}	X_{soot}	X_{minm}	X_{miam}	X_{micm}
0	Maritime	90	1	0.071	0.908	0.021	-	-	-	-	-
1	Continental	70	8	0.583	-	-	0.396	0.021	-	-	-
2	Biomass Burning	70	2	0.750	-	-	0.100	0.150	-	-	-
3	Desert	70	1	0.018	-	-	-	-	0.033	0.747	0.202
4	Desert	70	3	0.018	-	-	-	-	0.033	0.747	0.202
5	Desert	70	5	0.018	-	-	-	-	0.033	0.747	0.202

Table 3: Aerosol models parameters

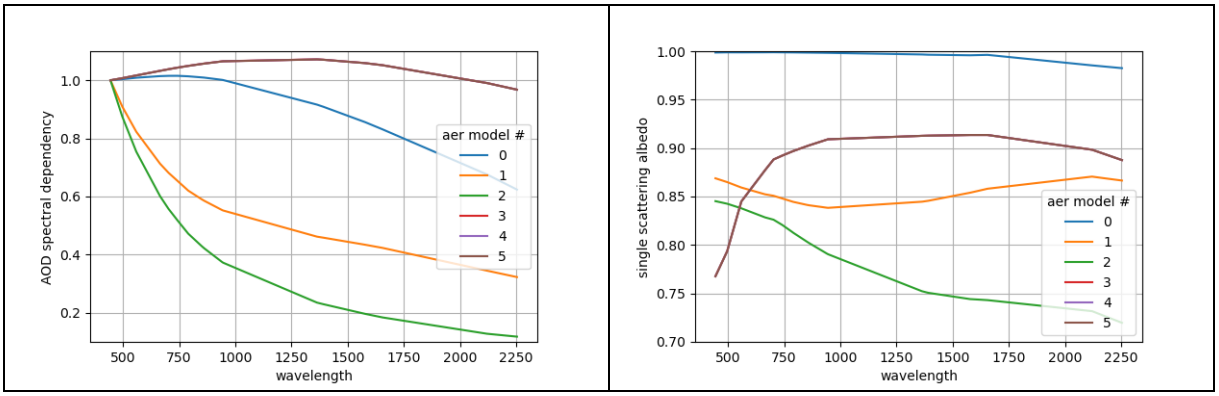

Figure 1: Aerosol models spectral optical properties: (left): Optical Depth, (right): Single Scattering Albedo

#0

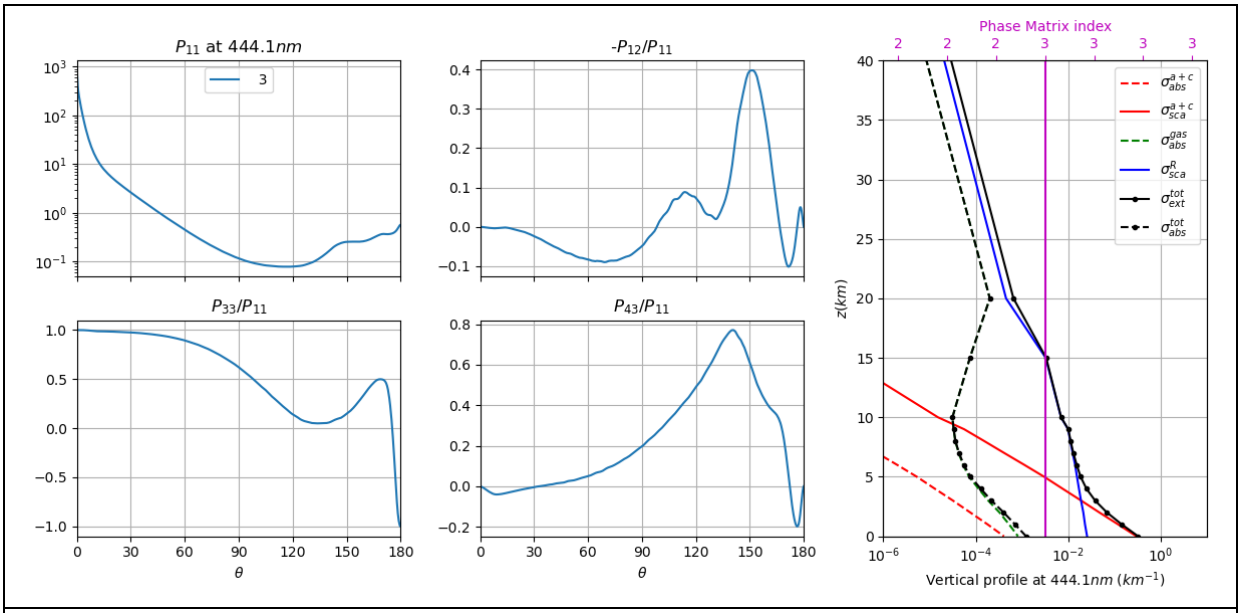
P_{11} at 444.1nm
3
$-P_{12}/P_{11}$
P_{33}/P_{11}
P_{43}/P_{11}
θ
Phase Matrix index
$z(km)$
σ_{abs}^{a+c}
σ_{sca}^{a+c}
σ_{abs}^{gas}
σ_{sca}^{R}
σ_{ext}^{tot}
σ_{abs}^{tot}
Vertical profile at 444.1nm (km^{-1})

#1

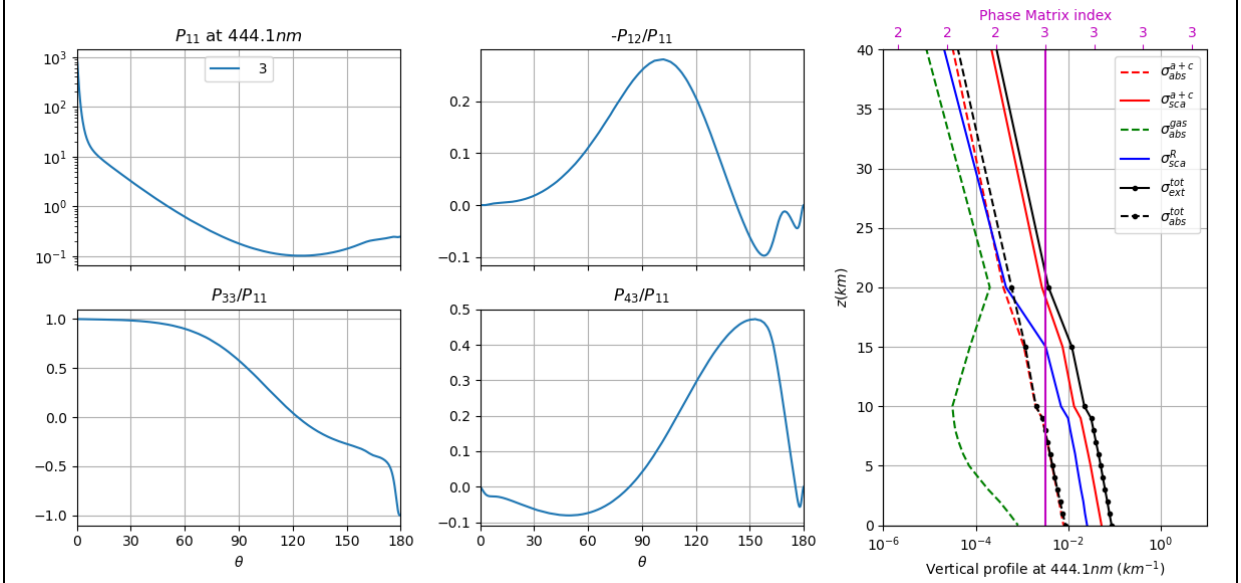
P_{11} at 444.1nm
3
$-P_{12}/P_{11}$
P_{33}/P_{11}
P_{43}/P_{11}
θ
Phase Matrix index
$z(km)$
σ_{abs}^{a+c}
σ_{sca}^{a+c}
σ_{abs}^{gas}
σ_{sca}^{R}
σ_{ext}^{tot}
σ_{abs}^{tot}
Vertical profile at 444.1nm (km^{-1})

#2

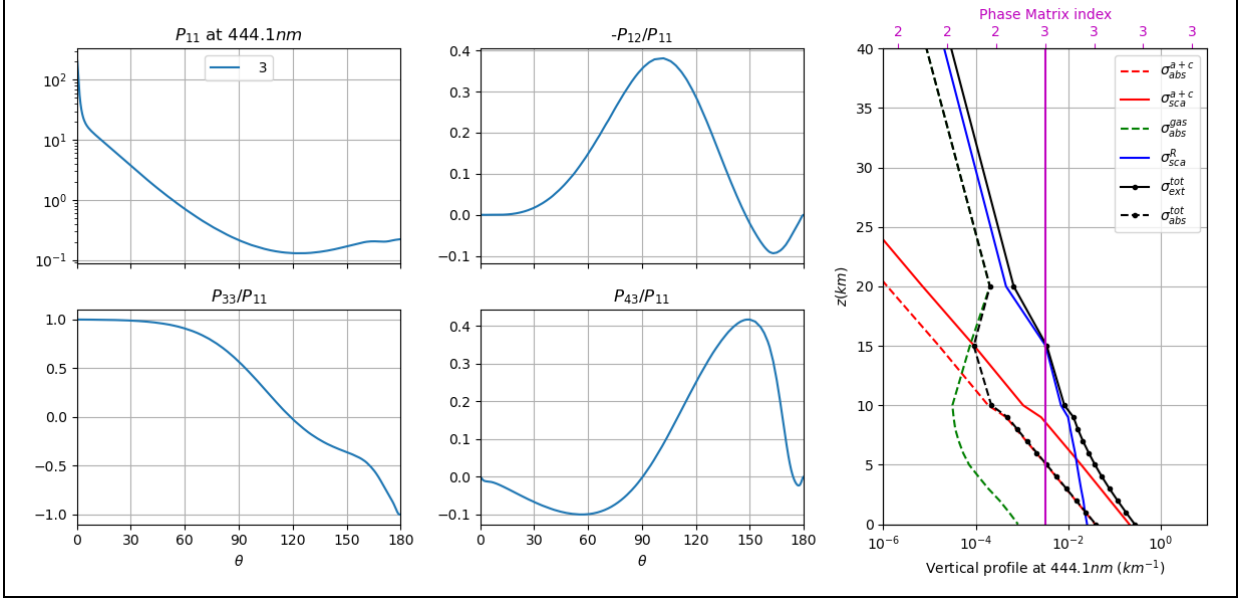
P_{11} at 444.1nm
3
$-P_{12}/P_{11}$
P_{33}/P_{11}
P_{43}/P_{11}
θ
Phase Matrix index
$z(km)$
σ_{abs}^{a+c}
σ_{sca}^{a+c}
σ_{abs}^{gas}
σ_{sca}^{R}
σ_{ext}^{tot}
σ_{abs}^{tot}
Vertical profile at 444.1nm (km^{-1})

#3

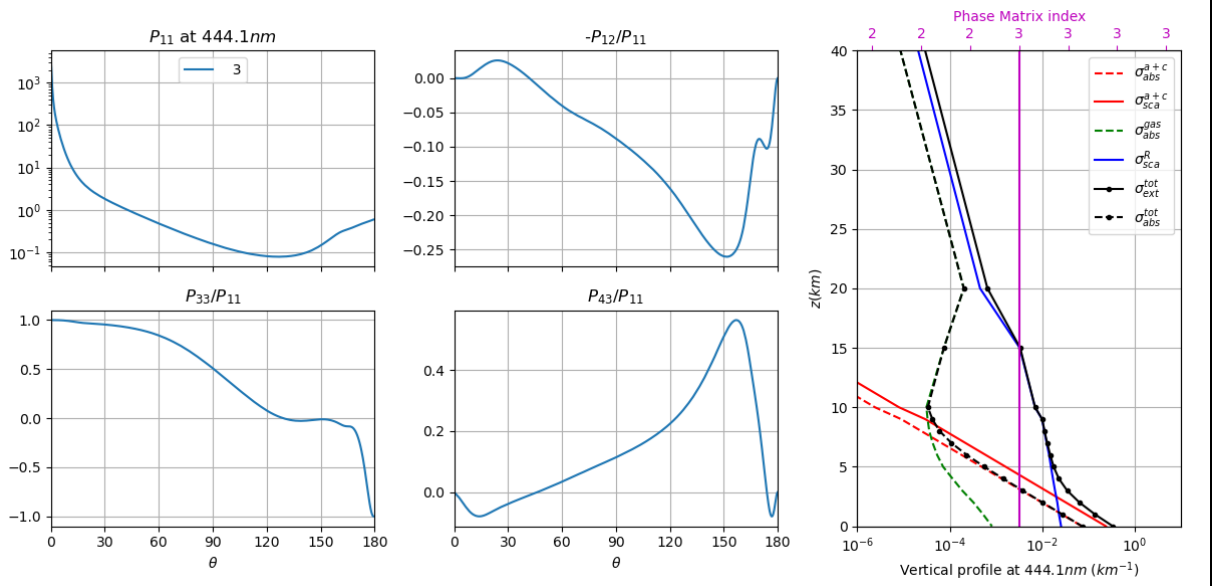
P_{11} at 444.1nm
3
$-P_{12}/P_{11}$
P_{33}/P_{11}
P_{43}/P_{11}
θ
Phase Matrix index
$z(km)$
σ_{abs}^{a+c}
σ_{sca}^{a+c}
σ_{abs}^{gas}
σ_{sca}^{R}
σ_{ext}^{tot}
σ_{abs}^{tot}
Vertical profile at 444.1nm (km^{-1})

#4

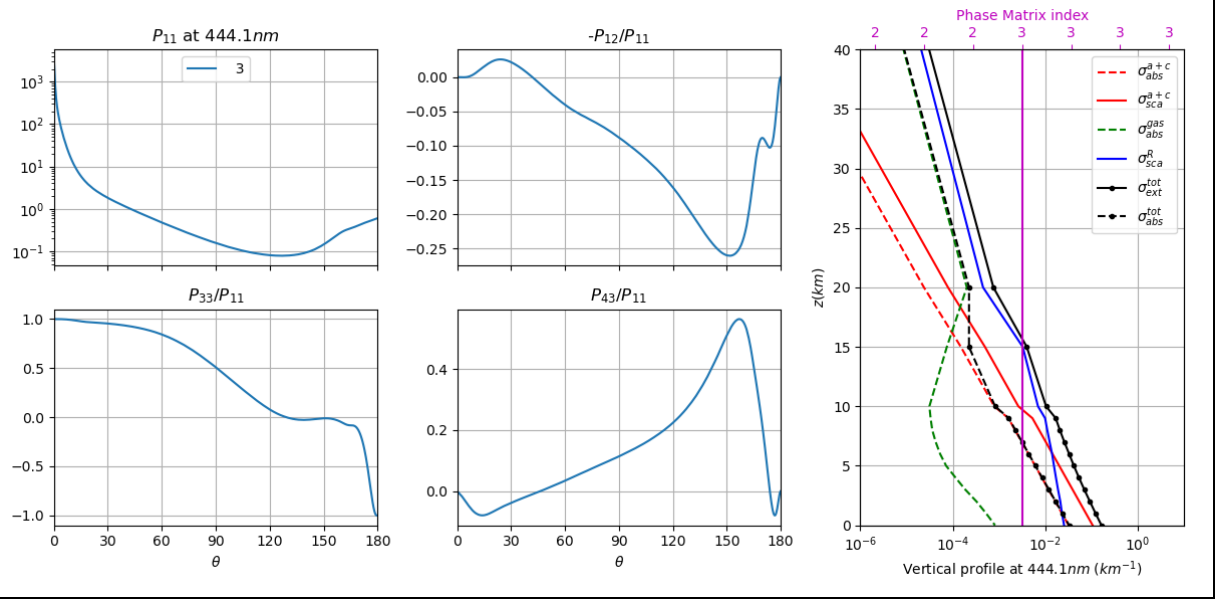
P_{11} at 444.1nm
3
$-P_{12}/P_{11}$
P_{33}/P_{11}
P_{43}/P_{11}
θ
Phase Matrix index
$z(km)$
σ_{abs}^{a+c}
σ_{sca}^{a+c}
σ_{abs}^{gas}
σ_{sca}^{R}
σ_{ext}^{tot}
σ_{abs}^{tot}
Vertical profile at 444.1nm (km^{-1})

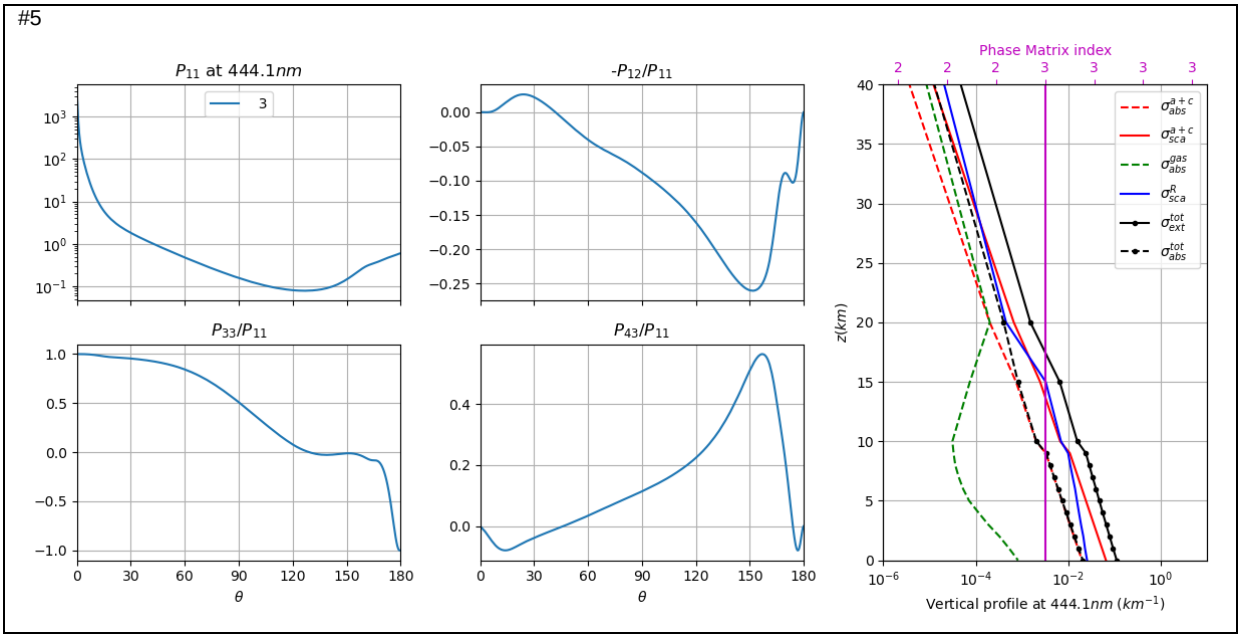

Figure 2: Aerosols Phase matrices (left) and atmospheric vertical profiles (right) for each of the 6 aerosols models and for a wavelength of 412.7 nm. The vertical profiles include: aerosol absorption (red dashed line), aerosol scattering (red solid line), gaseous absorption (green dashed line), Rayleigh scattering (blue solid line), total extinction (black solid line) and total absorption (black dashed line).

3.2.3 Ocean

In order to simulate a wide range of water spectrum we used the model of Park and Ruddick, 2005, implemented with a slight modification in POLYMER (Steinmetz and Ramon, 2018, Tan et al., 2019). The driving parameters are the Chlorophyll concentration and the SPM concentration. Two other dependent quantities are of interest:

f_b: which is the departure of particles scattering from pure Case I waters, it is defined as:

$$b_p^{550} = 0.416 * \ Chl^{0.766} * f_b$$

γ: it is the spectral slope of the particles backscattering:

$$b_{bp} = b_{bp}^{550} * \ (\frac{\lambda}{550})^{-\gamma}$$

#	0	1	2	3	4	5	6	7	8
Log_{10} (fb)	0.370	0.396	0.234	0.197	0.575	-0.366	0.925	1.351	1.705
Log_{10} (Chl)	-1.332	-0.761	-0.359	0.340	0.908	0.648	0.925	1.089	1.639
SPM	0.051	0.151	0.210	0.628	3.671	0.282	8.390	27.23	110.3
γ	3.75	2.78	2.10	0.93	0.00	0.40	0.00	0.00	0.00

Table 4: Marine models parameters (IOPs)

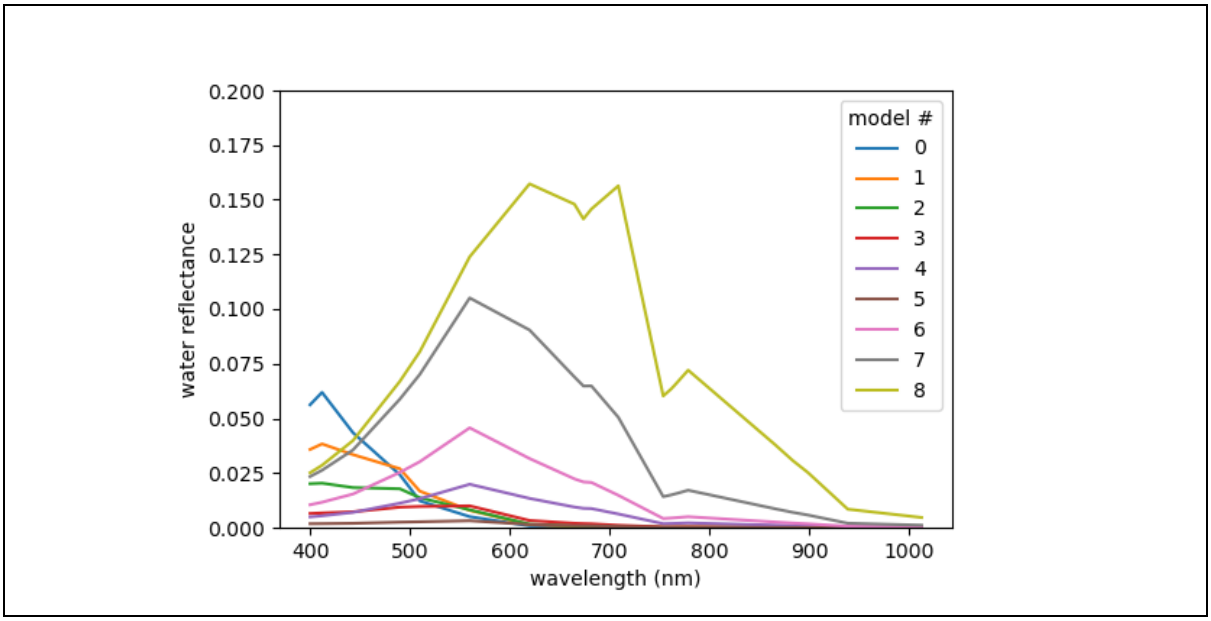

Figure 3: Water leaving reflectance just above the surface for the different water models listed in Table 4 and for a wind speed of 5 m/s.

The resulting water leaving reflectance

3.2.4 Surface albedos

For the description of the different surface albedos in this study we used the ECOSTRESS spectral library (Meerdink et al., 2019). We restricted ourselves to 4 different spectra, representative of both land surfaces and seafloors:

Type	ECOSTRESS reference	L	S
Snow	`water.snow.mediumgranular.medium.all.medgran_snw_.jhu.becknic`	x	
Sand	`soil.alfisol.paleustalf.none.all.87p2376.jhu.becknic`	x	x
Grass	`vegetation.grass.avena.fatua.vswir.vh352.ucsb.asd`	x	x
Rock	`rock.metamorphic.gneis.coarse.all.gneiss7.jhu.becknic`	x	x

Table 5: Type of surfaces used as boundary conditions in this study for the environment land surfaces (L) or seafloor (S)

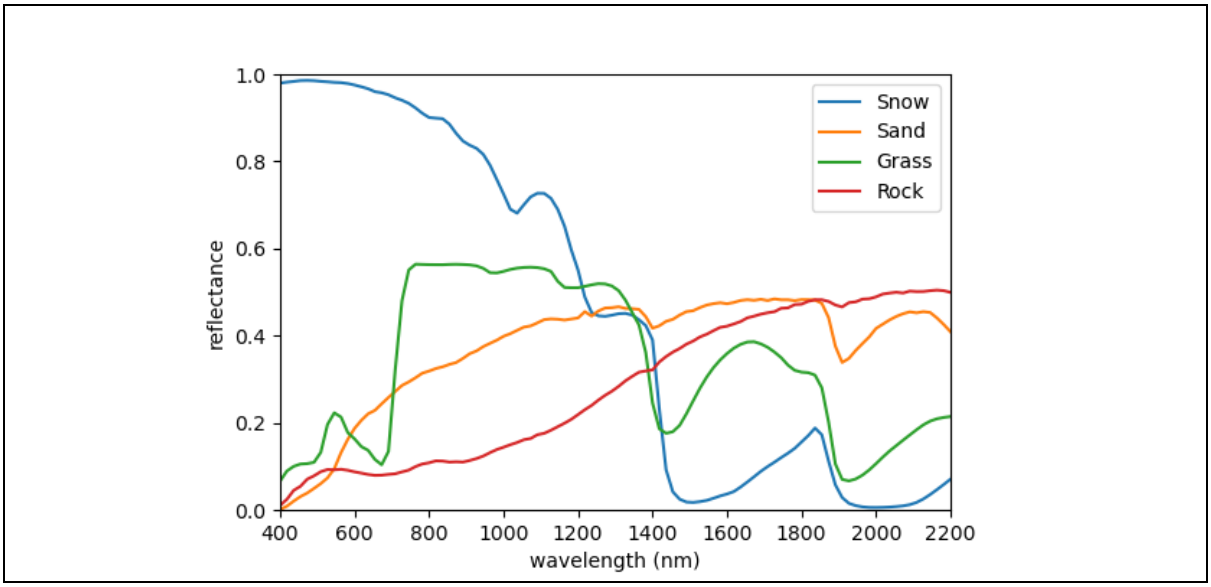

Figure 4: Spectral albedos of the different surfaces listed in Table 4

3.3 Scene Definitions

3.3.1 Geometry

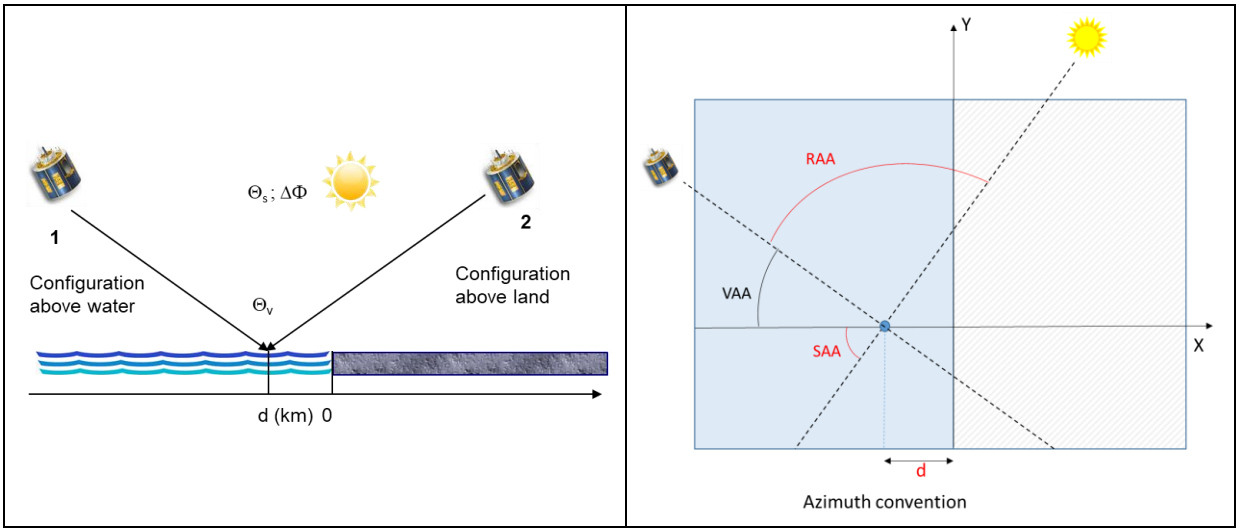

Figure 5: Angles definition

The typical scenes we want to characterize are those with (i) the ocean homogeneous case, (ii) a coastline in the vicinity of the water pixel or (iii) a water body surrounded by land. In the two last cases the distance to the coast *d* is the most relevant parameter. Thus we will simulate scenes of a pixel located at a varying distance to the coastline *d* or located at the center of a circular lake of radius *d*. From the literature we know that the influence of the environment will be in the range [0, 10km]. For off-nadir views the relative azimuth of the sensor relative to the coastline has also a significant influence, as when the sensor is located “above land”, more light reflected by the bright land surface is scattered into the sensor field of view and, therefore, the adjacency effects are more pronounced. We adopt the azimuth convention described in Figure 5 for the scenes with a linear coastline. We can summarize the logic of the geometries selected in this study:

For the ocean homogeneous case, coastline and lake scenes, we want to test:

- High and low SZA: 30 and 70°
- Nadir and S3/OLCI extreme oblique views thus VZA: 0 and 50°
- A relative azimuth between Sun and Sensor: principal plane and perpendicular to the principal plane: RAA: 0, 90, 180°. It corresponds to SAA: 0, 90, 180° for an arbitrary choice of VAA=0.
- In the case of coastline scenes we have to add the case VAA=180° for a configuration with the sensor “above land”.

3.3.2 Homogeneous scenes

The AOD at 550 nm is chosen between two values: 0.1 which is an average value and 0.5 above which we assume that the atmospheric corrections become inaccurate. Two wind speeds is enough to sample two extreme Fresnel interfaces. Table 6 summarizes the various parameters of this database of homogeneous cases. On Figure 6 is an example of TOA reflectance for S3/OLCI in a particular geometry for a set of water and aerosol models.

Parameter	**Size**	**Value**
Wavebands	21 10	OLCI: 21 bands MSI : 10 bands
Solar Zenith Angle θ_s (SZA)	2	30, 70 degrees
View Zenith Angle θ_v (VZA)	2	0, 50 degrees
Relative Azimuth Angle ϕ (RAA)	3	0, 90, 180 degrees
Aerosol Optical Depth $\tau_a(550)$	2	0.1, 0.5
Aerosol model	6	See Table 2
Wind speed	2	2, 12 m/s
Water reflectance model	9	See Table 3

Table 6: Parameters and size of the Homogeneous scenes database

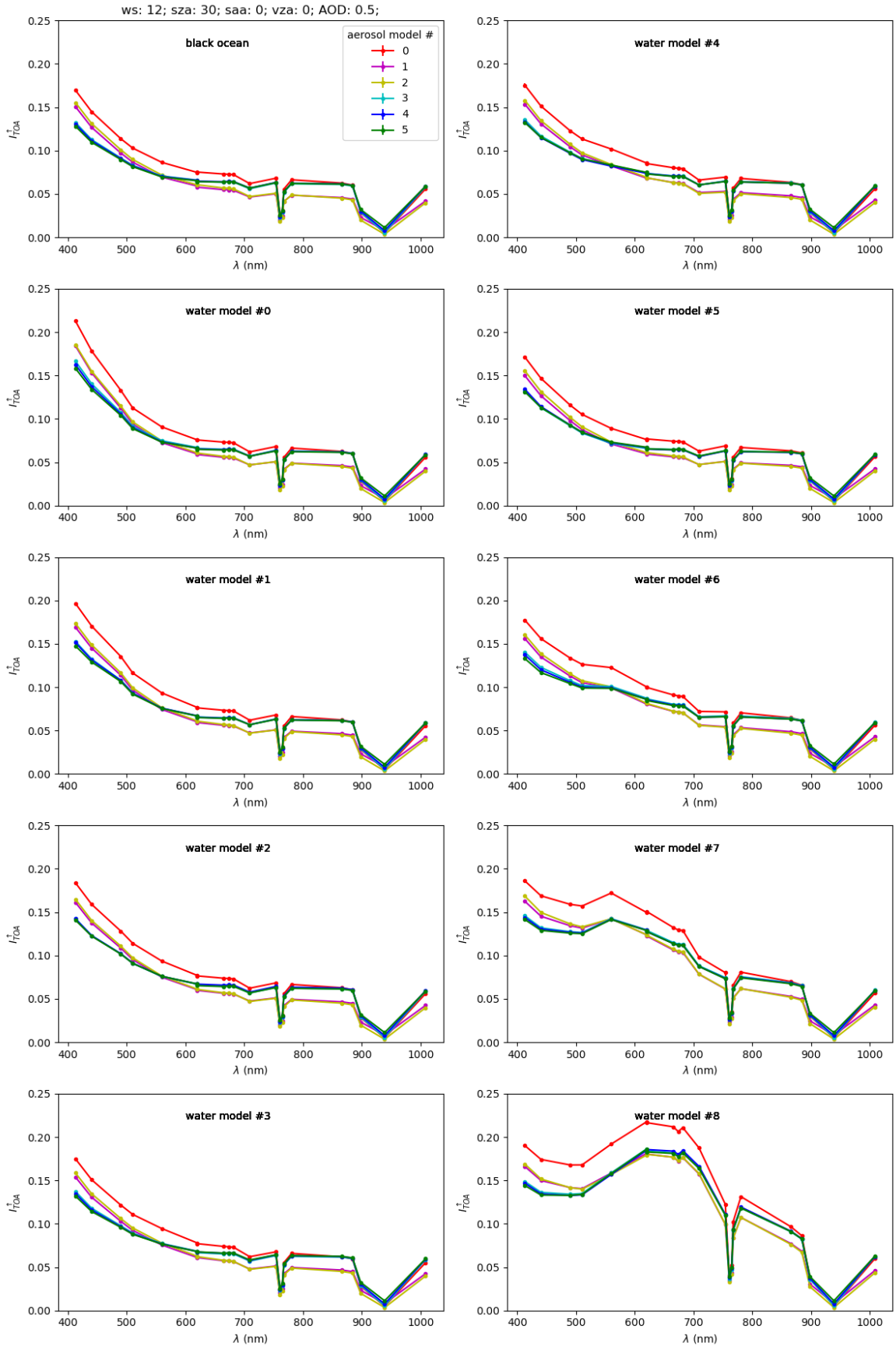

Figure 6: Output example of TOA reflectance spectra for OLCI in a particular geometry in the case of a homogeneous ocean scene, for all water models and aerosol models.

3.3.3 Adjacency effects

Adjacencies scenes are separated into two groups: the first one is for the coastline case and include a Solar Azimuth Angle dimension with two values 0 and 180° for a sensor 'above land' and 'above water' configuration. The distance d is sampled from one pixel (for OLCI: 250 m, for MSI, 25 m) to 10 km, which gives 4 values for OLCI and 6 for MSI. For the circular water body scenes, d represent the radius of the water body and the pixel simulated is located at the centre of the water body.

3.3.3.1 Coastline

Parameter	**Size**	**Value**
Albedo models for environment	4	Snow, Sand, Grass, Rock
Distance to a linear coast,	OLCI: 4 MSI : 6	250m, 1km, 2.5km, 10km 25m, 100m, 250m, 1km, 2.5km, 10km
Solar Azimuth Angle (SAA) (see azimuth convention on Figure 5)	2	0, 180 degrees

Table 7 : Same as Table 6 but for the coastline scenes

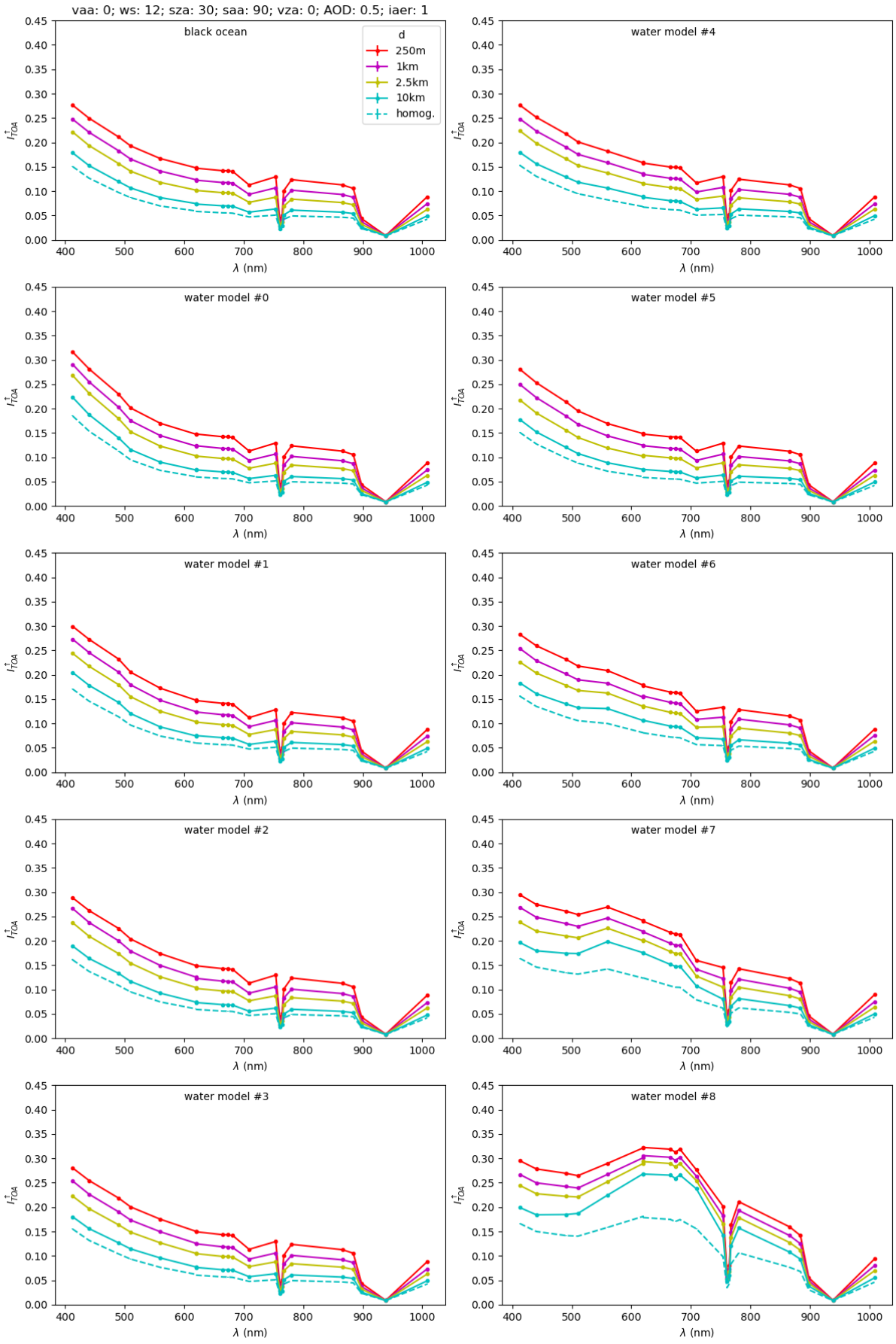
vaa: 0; ws: 12; sza: 30; saa: 90; vza: 0; AOD: 0.5; iaer: 1
black ocean
water model #4
water model #0
water model #5
water model #1
water model #6
water model #2
water model #7
water model #3
water model #8
d
250m
1km
2.5km
10km
homog.
$I^{\uparrow}_{TOA}$
λ (nm)

Figure 7 Output example of TOA reflectance spectra for OLCI in a particular geometry (nadir view) in the case of a coastline type scene, for all water models, one aerosol model and loading and as a function of the distance to the coast d. The land environment is 'SNOW'.

3.3.3.2 Circular water body

Parameter	**Size**	**Value**
Albedo models for environment	4	Snow, Sand, Grass, Rock
Radius of the water body	OLCI: 4 MSI : 6	250m, 1km, 2.5km, 10km 25m, 100m, 250m, 1km, 2.5km, 10km

Table 8 Same as Table 5 but for the water body scenes

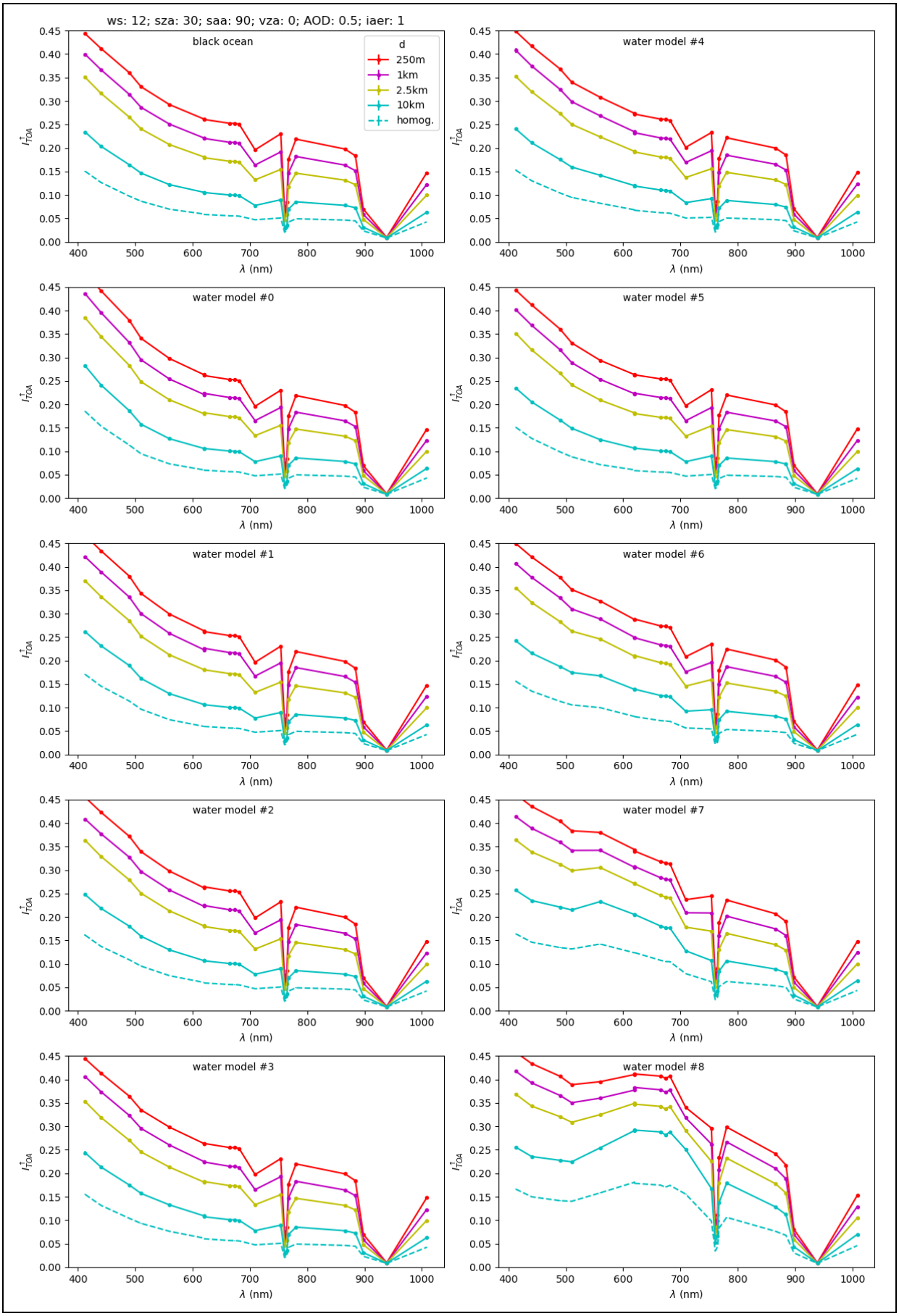

Figure 8 : Same as Figure 7 but for the Lake type scene.

3.3.4 Bathymetry effects

Parameter	Size	Value
Albedo models for seafloor	3	Sand, Grass, Rock
Depth	6	0.2m, 0.5m, 1m, 2m, 5m, 20m

Table 9 : Same as but for the bathymetry scene

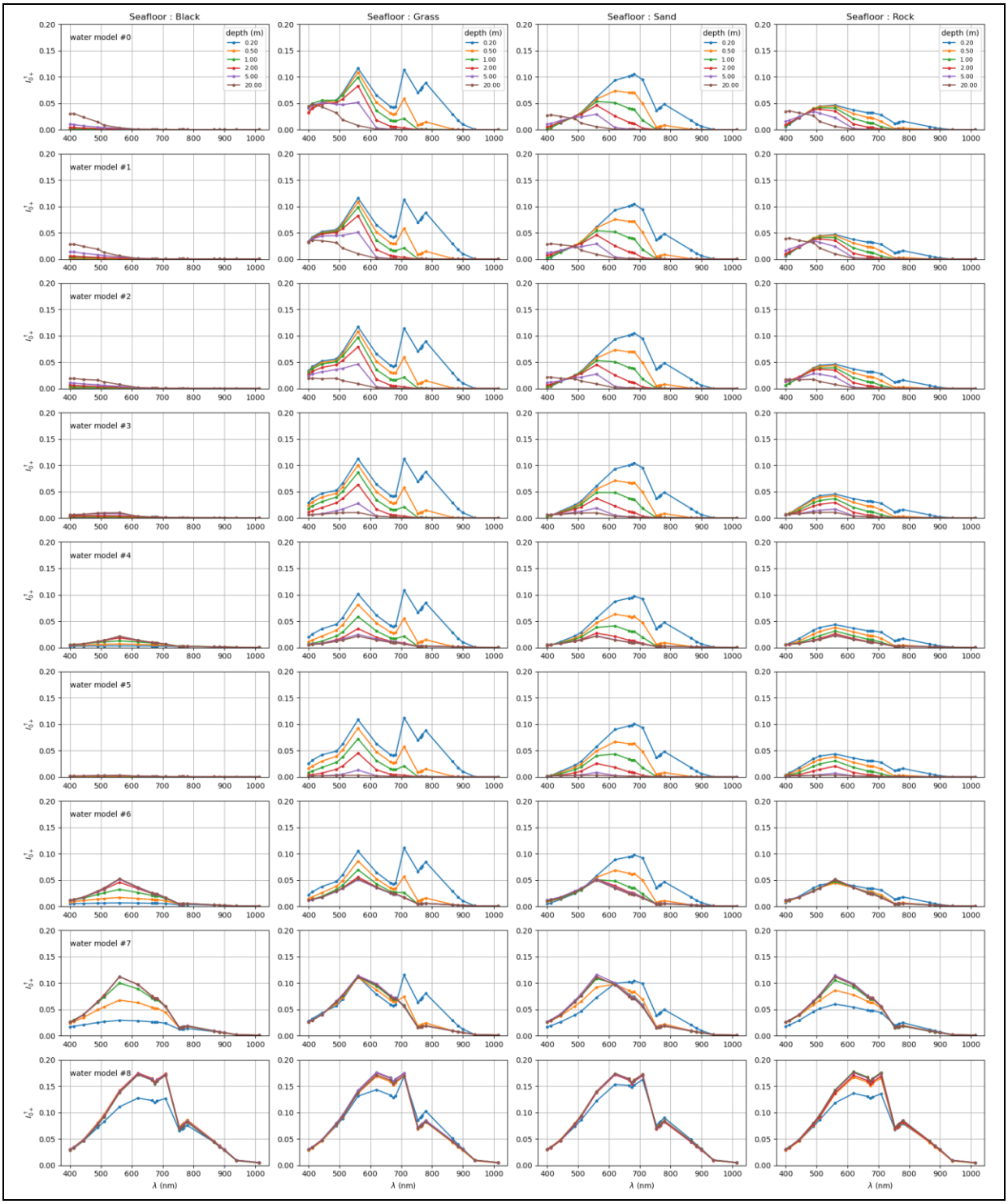

Figure 9 : Reflectance spectra for OLCI bands just above water (0+) for a particular geometry in the case of a varying seafloor spectrum and sea depth for all water models listed in Table 3. There is no atmosphere and the wind speed is 12 m/s

3.4 Database Format

All the datasets are stored in NetCDF format. The results for OLCI and MSI are separated. The files contain at least the dataset '`I_up (TOA)`' that is the TOA reflectance and sometimes also '`I_up (0+)`' for the reflectance just above the sea surface. The dimensions and values of the axes are those listed in Table 6, Table 7, Table 8, Table 9.

4 References

Chowdhary J., P.-W. Zhai, F. Xu, R. Frouin and D. Ramon (2020). Testbed results for scalar and vector radiative transfer computations of light in atmosphere-ocean systems. *Journal of Quantitative Spectroscopy and Radiative Transfer*, Volume **242**, doi: 10.1016/j.jqsrt.2019.106717.

Chowdhary J., Zhai P-W., Boss E., Dierssen H., Frouin R., Ibrahim A., Lee Z., Remer L. A., Twardowski M., Xu F., Zhang X., Ottaviani M., Espinosa W.R., and Ramon D. (2019), Modelling Atmosphere-Ocean Radiative Transfer: A PACE Mission Perspective. *Frontiers in Earth Science*, **7**:100. doi: 10.3389/feart.2019.00100.

Cox, C., & Munk, W. Measurements of the roughness of the sea surface from photographs of the Sun's glitter. Journal of the Optical Society of America, 44, 834-850, (1954).

Emde, C., Barlakas, V., Cornet, C., Evans, F., Korkin, S., Ota, Y., Labonnote, L. C., Lyapustin, A., Macke, A., Mayer, B., Wendisch, M., "IPRT polarized radiative transfer model comparison project – Phase A", *Journal of Quantitative Spectroscopy and Radiative Transfer*, **164**:8-36 (2015)

Emde, C., R. Buras and B. Mayer: "ALIS: An efficient method to compute high spectral resolution polarized solar radiances using the Monte Carlo approach", *Journal of Quantitative Spectroscopy and Radiative Transfer*, **112**, 1622-1631, (2011)

Frouin R., Ramon D., Boss E., Jolivet D., Compiègne M., Tan J., Bouman H., Jackson T., Franz B., Platt T., Sathyendranath S. (2018), Satellite Radiation Products for Ocean Biology and Biogeochemistry: Needs, State-of-the-Art, Gaps, Development Priorities, and Opportunities, *Frontiers in Marine Science*, **5**, pages 3, doi: 10.3389/fmars.2018.00003.

Frouin, R. J., B. A. Franz, A. Ibrahim, K. Knobelspiesse, Z. Ahmad, B. Cairns, J. Chowdhary, H. M. Dierssen, J. Tan, O. Dubovik, X. Huang, A. B. Davis, O. Kalashnikova, D. R. Thompson, L. R. Remer, E. Boss, O. Coddington, P.-Y. Deschamps, B.-C. Gao, L. Gross, O. Hasekamp, A. Omar, B. Pelletier, D. Ramon, F. Steinmetz, P.-W. Zhai, Atmospheric Correction of Satellite Ocean-color Imagery during the PACE Era, *Frontiers in Earth Science*, Vol. **7**, pages 145, https://doi.org:10.3389/feart.2019.00145, (2019).

Gasteiger, J., C. Emde, B. Mayer, R. Buras, S.A. Buehler, and O. Lemke, 2014: "Representative wavelengths absorption parameterization applied to satellite channels and spectral bands", *J. Quant. Spec. Rad. Transfer*, **148**, 99-115.

Hess, M., P. Koepke, and I. Schult, 1998: "Optical Properties of Aerosols and Clouds: The software package OPAC", *Bull. Am. Met. Soc.*, **79**, 831-844.

Kokhanovsky A.A., Budak V.P., Cornet C., Duan M., Emde C., Katsev I.L., Klyukov D.A., Korkin S.V., C-Labonnote L., Mayer., B., Min Q., Nakajima, T., Ota Y., Prikhach A.S., Rozanov V.V., Yokota T., Zege E.P.: Benchmark results in vector atmospheric radiative transfer, *J. Quant. Spectrosc. Rad. Transfer*, **111**, 1931-1946, doi: 10.1016/j.jqsrt.2010.03.005 (2010)

Marchuk, G. I., Mikhailov, G. A., Nazaraliev, M. A., "The Monte Carlo methods in atmospheric optics" Berlin Heidelberg, Springer-Verlag (1980)

Mayer, B., “Radiative transfer in the cloudy atmosphere”, *Eur. Phys. J. Conferences*, **1:75-99**, doi: 10.1140/epjconf/e2009-00912-1 (2009)

Meerdink, S. K., Hook, S. J., Roberts, D. A., & Abbott, E. A. (2019). The ECOSTRESS spectral library version 1.0. *Remote Sensing of Environment*, **230** (111196), 1–8.

Mishchenko, M. I., Travis. L. D., “Satellite retrieval of aerosol properties over the ocean using and polarization as well as intensity of reflected sunlight”, *J. Geophys. Res.*, **102**:16,989–17,013 (1997b)

Natraj, V. and Hovenier, J. W., “Polarized light reflected and transmitted by thick Rayleigh scattering atmospheres”, *The Astrophysical Journal*, **748**:28, 16pp, doi:10.1088/0004-637X/748/1/28 (2012)

Park, Y.-J. and Kevin Ruddick, "Model of remote-sensing reflectance including bidirectional effects for case 1 and case 2 waters," *Appl. Opt*. **44**, 1236-1249 (2005)

Plass, G. N., Kattawar, G. W., Guinn, J. A. Jr. “Radiative transfer in the Earth’s atmosphere and ocean: influence of ocean waves”, *Appl. Opt.*, **14**:1924–36. doi: 10.1364/AO.14.001924 (1975).

Ramon, D., Steinmetz, F., Jolivet, D., Compiègne, M., & Frouin, R. (2019). Modelling polarized radiative transfer in the ocean atmosphere system with the GPU-accelerated SMART-G Monte Carlo code. *Journal of Quantitative Spectroscopy and Radiative Transfer*, **222**, 89-107, doi: 10.1016/j.jqsrt.2018.10.017. https://www.hygeos.com/smartg

Ross, V., Dion, D., and Potvin, G. “Detailed analytical approach to the Gaussian surface bidirectional reflectance distribution function specular component applied to the sea surface”. *Journal of the Optical Society of America A*, **22**:2442–2453 (2005).

Santer, R., and C. Schmechtig, “Adjacency effect on water surfaces: primary scattering approximation and sensitivity study”, *Appl. Opt.*, **39**, 361-375 (2000)

Steinmetz F. and D. Ramon, “Sentinel-2 MSI and Sentinel-3 OLCI consistent ocean colour products using POLYMER”, PROCEEDINGS VOLUME 10778 SPIE ASIA-PACIFIC REMOTE SENSING | 24-26 SEPTEMBER 2018, doi: https://doi.org/10.1117/12.2500232.

Tan, J., Frouin, R., Ramon, D., Steinmetz, F. (2019), On the Adequacy of Representing Water Reflectance by Semi-Analytical Models in Ocean Color Remote Sensing. *Remote Sensing*, **11**, 2820.

Zawada, D., Franssens, G., Loughman, R., Mikkonen, A., Rozanov, A., Emde, C., Bourassa, A., Dueck, S., Lindqvist, H., Ramon, D., Rozanov, V., Dekemper, E., Kyrölä, E., Burrows, J. P., Fussen, D., and Degenstein, D.: Systematic Comparison of Vectorial Spherical Radiative Transfer Models in Limb Scattering Geometry, *Atmos. Meas. Tech. Discuss*. https://doi.org/10.5194/amt-2020-470, in **review**, 2021.